Optimal Design of Electrically Fed Hybrid Mars Ascent Vehicle

(Article begins on next page)

25 April 2024

Article

Optimal Design of Electrically Fed Hybrid Mars Ascent Vehicle

Lorenzo Casalino [†] , Filippo Masseni [†] and Dario Pastrone *,[†]

Dipartimento di Ingegneria Meccanica e Aerospaziale, Politecnico di Torino, Corso Duca degli Abruzzi, 24, 10129 Torino, Italy; lorenzo.casalino@polito.it (L.C.); filippo.masseni@polito.it (F.M.)
* Correspondence: dario.pastrone@polito.it
† These authors contributed equally to this work.

Abstract: The optimal design of the propulsion system for a potential Mars Ascent Vehicle is analyzed, in the context of the Mars Sample Return Mission. The Mars Ascent Vehicle has to perform an initial ascent phase from the surface and then circularize into a 170 km orbit. A two-stage launcher is taken into account: the same hybrid rocket engine is considered for both stages in order to limit the development costs. A cluster of two, three or four engines is employed in the first stage, whereas a single engine is always used in the second stage. Concerning the feeding system, three alternatives are taken into consideration, namely a blow down, a regulated and an electric turbo-pump feed system. The latter employs an electric motor to drive the oxidizer turbopump, whereas the power is supplied to the motor by lithium batteries. All the design options resulted in viable Mars Ascent Vehicle configurations (payloads are in the range of 70–100 kg), making the hybrid alternative worth considering for the sample return mission. The use of an electric turbo-pump feed system determines the highest vehicle performance with an estimated 10–25% payload gain with respect to gas-pressure feed systems.

Keywords: hybrid rocket engines; multidisciplinary optimization; robust optimization

1. Introduction

Hybrid Rocket Engines (HREs) are suitable for the replacement of both Solid Rocket Motors (SRMs) and Liquid Rocket Engines (LREs) in many applications [1–3] due to their high performance, which is close to that of storable liquid propellants. In addition, the physical separation of the solid fuel and the liquid oxidizer until ignition results in intriguing features, such as high safety and reliability, low costs of manufacturing and operation, throttle ability and shut-down/restart capabilities. In the present work, the feasibility of a hybrid powered Mars Ascent Vehicle (MAV) for the return of samples from Mars's surface is considered and analyzed.

The use of HREs has already been proposed for sample return missions [4–11], but at the moment, the baseline plan for the human exploration of Mars provides for only traditional liquid rocket propulsion [12]. The liquid propellant concept envisages the production in situ of the Liquid OXygen (LOX), employed as oxidizer, from carbon dioxide in Mars' atmosphere, whereas the liquid methane, used as fuel, is carried from Earth. An analogous concept can be used for an HRE employing in situ-produced LOX and paraffin-based wax as propellants [13,14].

On the other hand, the peculiar combustion process of hybrids bounds the solid fuel grain design and the oxidizer flow control strategy during operation. Given the propellant combination, the delivered specific impulse depends on the choice of chamber pressure and mixture ratio. The latter varies during operation because the fuel flow coming from the solid grain is a function of both grain port area and burning surface, which evolve even if a constant oxidizer mass flow is used. This phenomenon is the so-called mixture ratio shifting typical of HREs. The characteristics of the propellants combination (density, thermo-chemical properties as a function of the mixture ratio and

regression rate) are also of concern in the search for the optimal design, making the optimization process quite tricky. Moreover, a strict relationship exists between design trajectory and operation optimization in HREs due to their peculiar one-lever control mechanism. Therefore, a coupled optimization of the engine design and ascent trajectory is required and performed here by means of a hybrid optimization procedure that combines an indirect trajectory optimization method with a direct approach for the optimization of the engine design parameters [15].

In previous works, similar approaches have been applied aiming at the upgrade of existing launchers, and/or those under development, that use SRMs and/or storable LREs in the upper stages [2,3,16–18]. In Reference [19], different HRE design options (number of engines per stage, feed system, etc.) for MAV have been compared. In particular a simple blow-down type and a partially regulated system have been taken into account as feed system options. The use of electrically driven turbo-pump feed systems was beneficial, in terms of payload, when compared to simpler gas pressurized systems in previous hybrid applications [20,21]. In the proposed feed system, a battery-powered electric motor is used to drive a turbo-pump. Despite the relatively limited power and energy density of today's batteries, this solution has already been applied to bipropellant LREs, solving the small-scale turbine issues of gas cycles (e.g., see the Rutherford engine used to power the Rocket Lab's Electron launch vehicle [22,23]). Moreover, the use of electric pump is even more appealing for HREs, since the presence of just one liquid propellant makes it difficult to produce a working fluid for the turbine [24]. Thus, in the present work, the viability of a two-stage MAV for sample return mission is discussed, in which electric turbo-pumps are employed in the feed system. Benefits of electric turbo-pump feed systems with respect to gas-pressure feed systems are evaluated. Results are presented in Section 4 after presenting the needed modeling and optimization procedures in Sections 2 and 3.

2. Engine Design and Optimization

The chosen propellants combination is LOX/paraffin-based wax. This choice is driven by the large regression rate value and promising performance shown when employed in sounding rockets and upper stages [25,26]. Moreover, oxygen can be extracted from Mars' atmosphere, making in situ exploitation of resources a viable option.

A chamber pressure $p_c = 10$ bar is assumed in the evaluation of the performance of the propellants as the mixture ratio α varies [27]. Even though the actual chamber pressure can span over a wide range during engine operations, the error due to the constant-pressure assumption is small for the value of chamber pressures and mixture ratios considered in this work. The characteristic velocity c^* is evaluated assuming an ideal frozen equilibrium expansion, i.e., an isentropic expansion without changes in the chemical composition of the gas mixture throughout the nozzle. Moreover, a c^*-efficiency equal to 0.96 is introduced, taking into account the low overall combustion efficiency typical of HREs [28]. The dependence of the characteristic velocity c^* and the specific heat ratio γ on mixture ratio α is modeled by means of third-degree polynomial curves fitting, which are directly embedded in the code. Once the nozzle area expansion ratio and the ambient pressure are given, the thrust coefficient C_F can be computed assuming constant specific heat ratio, isentropic expansion and a 0.98 C_F-efficiency. The latter is introduced in order to take losses into account [28]. The relatively high regression rate of the chosen propellants combination allows for a cylindrical grain with a single circular port. A uniform regression rate along the port axis is considered, and its value is given by the time derivative of the port radius as reported in Equation (1).

$$\frac{\mathrm{d}R}{\mathrm{d}t} = a \left(\frac{\dot{m}_O}{A_p} \right)^n \propto \dot{m}_O^n \ R^{-2n} \tag{1}$$

where the coefficient $a = 7.00 \times 10^{-6}$ and exponent $n = 0.8$ when SI units are used [29,30]. The pyrolisis of the lateral ends of the grain is neglected. The presence of pressure losses inside the combustion chamber is taken into account by relating the chamber head-end pres-

sure p_1 to the chamber/nozzle stagnation pressure p_c by means of an approximate relation similar to that proposed by Barrere et al. for side-burning grains (see Equation (2)) [31].

$$p_1 = \left[1 + 0.2 \left(\frac{A_{th}}{A_p} \right)^2 \right] p_c \tag{2}$$

Equation (3) provides the oxidizer flow rate $\dot{m}_O$ during operation, under the assumption of constant hydraulic resistance Z in the oxidizer flow path from the tank and incompressible turbulent flow.

$$\dot{m}_O = \sqrt{(p_{fs} - p_1)/Z} \tag{3}$$

On the other hand, the fuel mass flow $\dot{m}_F$ and the propellant mixture ratio α are given by Equations (4) and (5).

$$\dot{m}_F = \rho_F A_b \frac{dR}{dt} \propto \dot{m}_O^n R^{1-2n} \tag{4}$$

$$\alpha = \frac{\dot{m}_O}{\dot{m}_F} \propto \dot{m}_O^{1-n} R^{2n-1} \tag{5}$$

The chamber stagnation pressure at nozzle entrance p_c is determined assuming an isentropic expansion as reported in Equation (6).

$$p_c = \frac{(\dot{m}_O + \dot{m}_F)c^*}{A_{th}} \tag{6}$$

Three options for the feed systems are considered: blow down, partially regulated and electric turbo-pump. In the partially regulated case, the burn starts with a constant tank pressure phase, followed by blow-down operation. Five parameters define the design of the HRE in the proposed ballistic model, namely initial thrust F_i (evaluated on Mars's surface), initial mixture ratio α_i, nozzle expansion ratio ϵ, initial value of feed system pressure $(p_{fs})_i$ and initial gas volume in the oxidizer tank (ullage volume) $(V_g)_i$. For the regulated feed system and the turbo-pump feed system, the initial ullage volume is fixed at 3% of the oxidizer volume in order to grant a regular response at engine ignition. The initial value of feed system pressure $(p_{fs})_i$ is equal to $(p_t)_i$ for the gas pressurized feed systems, whereas the initial discharge pressure provided by the pump $(p_d)_i$ has to be considered for the turbo-pump operation. In the partially regulated case, $(V_g)_i$ is replaced as optimization variable by $(m_O)_{bd}$, which stands for the amount of oxidizer that has been exhausted when the blow down phase starts (that is, the oxidizer exhausted during the regulated phase).

The initial value of the chamber pressure is fixed and such that $(p_c)_i = 0.4 \, (p_{fs})_i$. During operation, the actual ratio p_{fs}/p_c is not constant, but the assumed initial ratio is able to grant $p_{fs}/p_c > 1.5$ for the whole engine burn, avoiding the coupling between the engine and the oxidizer feed system. In order to avoid excessive pressure losses and nonuniform grain regression, a fixed value of the initial port area to throat area $J = 0.5$ is assumed, although a larger value could result in better performance. The optimized initial thrust was shown to be very large in preliminary calculations. Therefore, F_i was dropped from the optimization parameters and its value was imposed.

Given the aforementioned set of design parameters, the engine and grain initial characteristics and performance are determined. The initial values of c^* and γ at engine ignition are given by α_i, and p_e/p_c can be computed from ϵ. Knowing the ambient pressure p_0, the thrust coefficient C_F and $c = c^* C_F$ can then be calculated. The initial thrust F_i fixes the propellants mass flow rates at ignition as reported by Equation (7).

$$(\dot{m}_p)_i = (1 + \alpha_i)(\dot{m}_F)_i = \frac{1 + \alpha_i}{\alpha_i}(\dot{m}_O)_i = \frac{F_i}{c_i^*(C_F)_i} \tag{7}$$

The throat area A_{th} can be determined from the aforementioned Equation (6). In this context, throat erosion effects are neglected, and thus A_{th} = constant. This assumption is adopted due to the preliminary nature of the present analysis, albeit easily managed by the proposed optimization procedure [25,26]. The initial port area and radius are calculated as $(A_p)_i = \pi R_i^2 = A_{th}/J$ and the initial burning area $(A_b)_i$ is determined from Equation (4). The grain length L_b is obtained as reported in Equation (8), completely specifying the initial grain geometry.

$$L_b = (A_b)_i/(2\pi R_i) \tag{8}$$

The feed system pressure p_{fs} rules engine operation. During blow down operation, it is calculated assuming an isentropic expansion of the pressurizing gas in the tank, as described by Equation (9).

$$p_{fs} = (p_t)_i \left[\frac{(V_g)_{bd}}{V_g} \right]^{\gamma_g} \tag{9}$$

where $(V_g)_{bd}$ is the auxiliary gas volume in the propellant tank at the start of the blow-down phase, and V_g is its value at the generic time t. In the simpler blow-down feed system, one has $V_g = (V_g)_i + m_O/\rho_O$ and $(V_g)_{bd} = (V_g)_i$, whereas $(V_g)_{bd} = (V_g)_i + (m_O)_{bd}/\rho_O$ when the regulated feed system is considered.

In the turbo-pump feed system, an electric motor drives the pump that feeds the oxidizer into the combustion chamber. The power available is assumed as constant during operation and thus determined by Equation (10), considering the initial values of discharge pressure $p_{fs} = (p_d)_i$ and oxidizer flow rate $\dot{m}_O = (\dot{m}_O)_i$.

$$P_e = \frac{\dot{m}_O(p_{fs} - p_t)}{\rho_O \eta_{ep}} = \text{constant} \tag{10}$$

In this context, the authors assume $p_t = 1$ bar = constant during operation and neglect the small amount of pressurizing gas mass required to keep p_t constant during engine burn. The pump power is held as fixed during operation, and Equation (10) provides the feed pressure $p_{fs} = p_d$ as a function of the oxidizer flow rate. Thus, in the electric turbo-pump case, the number of the optimization variable is equal to four, because $(V_g)_i$ is fixed and no additional parameters are required to determine the oxidizer flow rate during operation. In the conversion process of electrical energy into flow head rise, the authors assume an overall efficiency $\eta_{ep} = 0.53$ [32].

Solid fuel geometry and oxidizer-exhausted mass can be computed by the numerical integration of Equations (1) and (3) during engine operation, also providing the tank pressure in the gas-pressurized cases. The regression rate, the propellant flow rates (and their ratio α), p_c and p_1 are determined numerically by solving Equations (1)–(6) and using the fitting for c^* as a function of α. The thrust level $F = p_c A_{th} C_F$ is calculated once C_F is known at the actual altitude, allowing for trajectory integration. One can then compute the grain outer radius $R_f = R_i + w$ and the grain web thickness w at engine burnout. At this point, the overall propellant mass is known and structural masses can be estimated in order to compute the launcher payload, which is the optimization merit function to be maximized.

The engine and stage length is given by the sum of the lengths of oxidizer tank, grain and nozzle. In addition, the helium tank comprises the regulated feed system. A 1-mm-thick cylindrical aluminum casing encapsulates each stage, and the case diameter is fixed by the oxidizer tank diameter, which is assumed as equal to the combustion chamber diameter in the blow down case or to the auxiliary gas tank diameter in the regulated case. A 6 mm insulating liner (with density equal to that of the solid fuel) is taken into account in the combustion chamber, together with an aluminum alloy cylindrical wall. Aluminum is also employed for the cylindrical oxidizer tank. The walls' thicknesses are determined to withstand the internal pressure in the oxidizer tank and combustion chamber, assuming a safety factor equal to 1.25. In addition, a lower limit of 0.5 mm is imposed. A 45 deg convergent and a 20 deg divergent nozzle are taken into account, assuming a phenolic

silica ablative layer. The thickness is considered as uniform and evaluated according to Reference [33]. The ablative layer mass estimation is conservative, and thus the small nozzle structural mass is negligible. In the end, the authors neglect the mass of interstage adapters and separation mechanism. It is worth noting that different architectures could be considered for the engine (e.g., multiple oxidizer tanks surrounding the combustion chamber, instead of a single tank stacked on top of it) characterized by different values of the dry mass. The optimization of the system architecture is assumed to be a possible growth margin whose evaluation is beyond the scope of the present article, which only aims at demonstrating the feasibility of a hybrid MAV and evaluating benefits derived from the use of electric turbo-pumps.

In the electric turbo-pump feed system, the power required by the electric motor that drives the pump is provided by batteries. The masses of the pump, electric motor and batteries are calculated by means of typical power density (power to mass ratio) values, which are provided by existing literature. The electric motor and pump mass are evaluated as reported in Equation (11), where $P_{e,max} = P_e = $ constant is the maximum electrical power required, which is given by the initial discharge pressure (which is an optimization variable) and oxidizer flow rate at ignition.

$$m_{ep} = \frac{P_{e,max}}{\delta_{ep}} \tag{11}$$

$\delta_{ep} = 3.92$ kW/kg has been assumed for the evaluation of the electric drive system plus the pump mass [32]. The batteries' mass is constrained by the most stringent between two requirements: the maximum electrical power required $P_{e,max} = P_e = $ constant and the total electrical energy $E_{e,tot}$ needed to drive the pump for the whole engine burning time t_{burn}, which is given by Equation (12).

$$E_{e,tot} = \int_0^{t_{burn}} P_e dt = P_{e,max} t_{burn} \tag{12}$$

The batteries' mass can thus be evaluated by means of Equation (13), where a power density $\delta_{bp} = 6.95$ kW/kg, an energy density $\delta_{be} = 198.5$ Wh/kg (energy-to-mass ratio) and a safety factor of 1.2 are considered [32].

$$m_b = 1.2 \max \left(\frac{P_{e,max}}{\delta_{bp}}, \frac{E_{e,tot}}{\delta_{be}} \right) \tag{13}$$

The reader can notice that the power-constrained mass is known before the actual trajectory is optimized, depending only on the pump power level, which in turn is a function of the initial discharge pressure (i.e., of a design variable). On the contrary, the energy-constrained mass has to be computed "a posteriori" because the actual burning time is not know before trajectory optimization. For this reason, a characteristic burn time $t_{burn}^* = \delta_{be}/\delta_{bp}$ is defined, which represents the simultaneous fulfillment of both constraints. The battery mass is given by the power constraint when $t_{burn} \leq t_{burn}^*$ (i.e., shorter missions), whereas the energy constraint is binding when $t_{burn} \geq t_{burn}^*$ (i.e., longer missions). In the latter case, the batteries' mass has to be checked "a posteriori" to take into account the energy surplus required.

A direct method optimizes the engine design parameters once initial tentative values for the design parameters are provided [34]. Then, given the engine design, the fast and accurate indirect procedure computes the optimal trajectory, and the corresponding payload is known. The computation of engine design and optimal trajectory for a given set of design parameters requires only few seconds on a modern personal computer. The initial values of the design parameters are then varied by small quantities in order to numerically evaluate the derivatives of the performance index (i.e., launcher payload) with respect to the design parameters. A procedure based on Newton–Raphson's method is employed in

the determination of the set of design parameters that simultaneously nullify every index partial derivatives. Only a few minutes are required to obtain the optimal design and the corresponding optimized trajectory.

3. Rocket Configurations and Trajectory Optimization

In this work, a two-stage MAV is considered, and the same HRE is employed in both the stages. N_1 engines are used in the first stage, where $N_1 = 2, 3, 4$, whereas a single HRE is present in the second stage (i.e., $N_2 = 1$). This strategy allows for a reduction in the development cost of the hybrid engines when compared to the use of different engines in each stage.

The ascent trajectory is split into several phases: (1) vertical ascent (followed by an instantaneous velocity rotation) and (2) zero-lift gravity-turn ascent until the first stage is exhausted and jettisoned (3) coast arc and (4) second-stage burn with optimal thrust direction until insertion into the desired orbit. Phases (2) and (4) are further divided into two sub-phases when the regulated feed system is employed, corresponding to constant tank pressure, i.e., (2a) and (4a), and then blow down engine operation, i.e., (2b) and (4b). The optimization aims at the maximization of the launcher payload mass μ, which is equal to the second-stage final mass minus its inert mass. The j-th phase starts at time t_{j-1} and ends at t_j. The launcher is modeled as a point-mass rocket, and the state equations in an inertial Mars-centered reference frame, coded in non-dimensional form to improve the integration numerical accuracy, are: improve the integration's numerical accuracy, are

$$\frac{\mathrm{d}\boldsymbol{r}}{\mathrm{d}t} = v\boldsymbol{s}. \qquad \frac{\mathrm{d}\boldsymbol{v}}{\mathrm{d}t} = -\frac{\boldsymbol{r}}{|\boldsymbol{r}|^3} + \frac{\boldsymbol{F} - \boldsymbol{D}}{m} \qquad \frac{\mathrm{d}m}{\mathrm{d}t} = -\frac{F}{c} \qquad (14)$$

where an inverse-square gravity field is assumed and $D = (1/2)\rho_{atm}C_D S v_{rel}^2$ is the aerodynamic drag, which is regarded as independent from the value of the payload mass in the present approach. For each sub-rocket, the reference cross section is a function of the rocket diameter d and the number of hybrid engines N, i.e., $S = N\pi d^2/4$. The aerodynamic drag coefficient C_D of both stages is calculated as a function of the Mach number by means of the typical law for rockets reported in Figure 1.
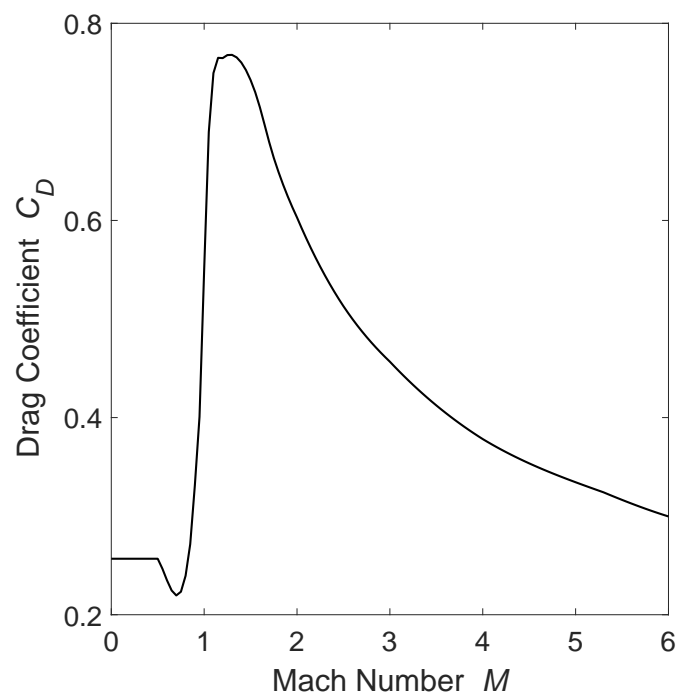

Figure 1. Drag coefficient.

It is worth noting that, due to the thinness of Mars's atmosphere, the drag influence on rocket performance is practically negligible. The relative velocity can be computed as $\boldsymbol{v}_{rel} = \boldsymbol{v} - \boldsymbol{\omega} \times \boldsymbol{r}$, where $\boldsymbol{\omega}$ stands for Mars's angular velocity. The thrust F is written as a function of the vacuum thrust F_{vac} as reported in Equation (15), where, once the engine design has been specified, F_{vac} is a given function of time.

$$F = F_{vac} - \epsilon A_{th} p_{atm} \tag{15}$$

The computation of aerodynamic drag D and thrust F require the knowledge of ambient density ρ_{atm} and pressure p_{atm}, respectively, as functions of rocket altitude h. Thus, the authors employ numerical fits of pressure and temperature of Mars's atmosphere according to a simplified model. These fits are reported as Equations (16) and (17), where SI units (K, Pa and m) are employed. The atmospheric density is then computed by means of the perfect gas equation.

$$T = \begin{cases} 242.15 - 0.000998 \, h, & \text{when } h \le 7000 \text{ m} \\ 249.75 - 0.00222 \, h, & \text{when } h > 7000 \text{ m} \end{cases} \tag{16}$$

$$p = 699\exp(-0.00009 \, h) \tag{17}$$

The initial values (i.e., at $t_0 = 0$) of the problem state variables (position, velocity and rocket mass) and the altitude at the end of the first phase (vertical ascent) are prescribed by the problem boundary conditions, whereas at the final time t_f, a circular orbit of assigned altitude is imposed. The use of the same engine in both stages introduces the additional condition $t_4 - t_3 = t_2 - t_0$ because the burning time of the first and second stage must be equal. In addition, $t_{3a} - t_3 = t_{2a} - t_0$ is added, to the boundary conditions when the regulated feed system is employed.

Given the engine performance, the optimal trajectory is found applying the theory of optimal control. Adjoint variables are associated to the state equations and the Hamiltonian, whose formal expression depends on the phase of flight, can be written as reported in Equation (18).

$$H = \lambda_r vs. + \lambda_v \left(\frac{\boldsymbol{r}}{|\boldsymbol{r}|^3} + \frac{\boldsymbol{F} - \boldsymbol{D}}{m} \right) - \lambda_m \frac{F}{c} \tag{18}$$

Euler–Lagrange equations are then provided by the Optimal Control Theory (OCT) for the adjoint variables, as shown in Equation (19).

$$\frac{d\lambda_r}{dt} = -\frac{dH}{d\boldsymbol{r}} \qquad \frac{d\lambda_v}{dt} = -\frac{dH}{d\boldsymbol{v}} \qquad \frac{d\lambda_m}{dt} = -\frac{dH}{dm} \tag{19}$$

In this work, the thrust is vertical during phase (1), parallel to the relative velocity during phase (2), zero during phase (3) (coasting) and free and optimized during phase (4). The thrust direction during phase (4) is provided by the OCT, which is shown to be parallel to the velocity adjoint vector, also named the primer vector. Boundary conditions for optimality, at the initial and final point and at the boundaries of each phase, are given by the OCT [35]. The velocity adjoint vector must be parallel to the velocity vector just after the velocity turn. Moreover, the transversality conditions are provided by the OCT and allow for the determination of the relevant times. The latter are somewhat complex because thrust and specific impulse are time-dependent in HREs. Thus, their derivation is detailed in the following. The time dependencies of vacuum thrust and specific impulse make the Hamiltonian not constant, and additional virtual equations for F_{vac}, c, p_{fs} and port radius R are introduced (see Equations (20)–(23)),

$$\frac{\mathrm{d}F_{vac}}{\mathrm{d}t} = f_F(p_{fs}, R) \tag{20}$$

$$\frac{\mathrm{d}c}{\mathrm{d}t} = f_c(p_{fs}, R) \tag{21}$$

$$\frac{\mathrm{d}p_{fs}}{\mathrm{d}t} = f_p(p_{fs}, R) \tag{22}$$

$$\frac{\mathrm{d}R}{\mathrm{d}t} = f_R(p_{fs}, R) \tag{23}$$

where the fucntions in the RHS of Equations (20)–(23) are given, albeit implicit, functions of R and p_{fs}. Then, the augmented Hamiltonian can be defined as $H' = H + \lambda_F f_f + \lambda_C f_C + \lambda_p f_p + \lambda_R f_R$, and the related transversality conditions are reported as Equation (24).

$$H'_{2-} - H'_{2+} + H'_4 = 0 \qquad H'_{3-} - H'_{3+} + H'_4 = 0 \tag{24}$$

This formulation makes the augmented Hamiltonian explicitly independent from time and therefore piecewise constant. One has $H'_{2+} = H'_{3-}$ and $H'_{3+} = H'_4$ and the transversality conditions become $H'_{3-} = 0$ and $H'_{2-} + H'_4 = 0$. F_{vac}, c, p_{fs}, and R do not appear in the boundary conditions at t_2 and t_4; thus, the corresponding adjoint variables are null and $H' = H$. Hence, the aforementioned transversality conditions are equivalent to $H_{3-} = 0$ (i.e., the Hamiltonian is zero during the coast arc) and $H_{2-} + H_4 = 0$ (i.e., the Hamiltonian has the same magnitude but different sign at the end of the burns). In the end, it is worth noting that the evaluations of the augmented Hamiltonian and of the additional adjoint variables are actually not necessary. The application of the OCT generates a multipoint boundary value problem, which is solved by a procedure based on Newton's method [36].

4. Results

Concerning the roadmap for Mars exploration, the return of a sample from the surface of Mars would be a milestone and a very important scientific achievement. The use of HREs has been already proposed in the past [4–11], and the comparison of several design options is the main focus of the present work. The initial mass of the MAV is here fixed and equal to 500 kg, whereas the expected payload is expected to be in the 75–100 kg range. Motion on the Mars equatorial plane and ascent to a 170 km circular orbit are considered. The best value of N_1 has been discussed in a previous work on the same topic and was shown to fall between 2 and 3 for the sample return mission [19]. In addition, $N_1 = 4$ is investigated in the present work. The three feed systems, described in the previous sections, are analyzed, and their performance is compared. Tables 1 and 2 report the launcher mass budget and performance. The length-to-diameter ratio of each stage is below 10 for every feed system and first-stage option, allowing for vertically stacked stages.

Concerning the gas-pressurized systems, the highest payload masses are obtained for $N_1 = 2$ and 3, when the blow-down and regulated feed systems are, respectively, used. $N_1 = 4$ solutions exhibit for both cases reduced velocity losses and smaller dry mass for the single HRE used in the stage. However, the most relevant effect is related to the non-uniform acceleration distribution, thus resulting in lower performance in terms of payload for $N_1 = 4$. The use of a regulated feed system improves the performance with respect to the blow down case due to the lower dry mass. This improvement is mainly due to the lower initial tank pressures, which allows for lighter oxidizer tanks. Moreover, the use of the regulated system results in a less-steep ascent trajectory during the constant pressure operation with respect to the blow down cases, which is more efficient in terms of velocity losses. The mixture ratio shifting is present in both blow-down and regulated solutions, albeit being more severe in the regulated case, as reported in Figure 2.

The electric turbo-pump feed system further reduces the system dry mass and improves the payload due to the absence of pressurization in the oxidizer tanks, despite the

additional masses of the electric components required. The highest payload is obtained for $N_1 = 3$, as in the regulated case. The initial thrust of this solution is far greater than blow-down or regulated ones, as reported in Figure 3. This optimization strategy seems to be caused by the relatively small increase in electric components masses resulting from high thrust levels, whereas an analogous strategy would be extremely penalizing in terms of engine dry mass in the gas-pressurized cases. As a consequence, the engine burn is shorter and the trajectory steeper, as shown in Figure 4, resulting in relevant decreases in gravitational and aerodynamic losses (see the last column of Table 1).

Table 1. Overall MAV mass budget and performance. BD, R and TP stand for blow down, regulated and turbo pump feed system, respectively.

Case	μ	m_p	m_{dry}	α_{avg}	Isp_{avg}	V_{losses}
-	kg	kg	kg	-	s	km/s
2 + 1 BD	75.03	345.81	79.16	2.062	298.1	0.794
3 + 1 BD	74.77	339.81	85.42	2.038	298.7	0.710
4 + 1 BD	72.29	337.79	89.17	2.024	298.0	0.671
2 + 1 R	86.25	345.95	67.80	2.071	296.9	0.672
3 + 1 R	86.73	340.60	71.85	2.053	297.7	0.591
4 + 1 R	84.82	338.17	76.15	2.038	298.3	0.554
2 + 1 TP	93.04	348.78	58.18	2.128	290.9	0.665
3 + 1 TP	100.91	335.24	63.85	2.152	293.2	0.487
4 + 1 TP	99.81	331.70	68.49	2.191	294.4	0.425

Table 2. Hybrid engine design. BD, R and TP stand for blow down, regulated and turbo pump feed system, respectively. The sixth column (m_e) reports the sum of electrical components masses (motor, pump and batteries) when the turbo pump feed system is employed.

Case	α_i	$(p_{fs})_i$	$(V_g)_i$	V_{He}	m_e	ϵ	d	L_{cc}	L_t	L_n
-	-	bar	m^3	m^3	kg	-	m	m	m	m
2 + 1 BD	1.53	21.4	7.1×10^{-2}	-	-	17.8	0.31	0.61	1.97	0.40
3 + 1 BD	1.44	21.5	5.5×10^{-2}	-	-	18.8	0.36	0.53	1.74	0.36
4 + 1 BD	1.39	20.9	4.4×10^{-2}	-	-	18.1	0.33	0.48	1.58	0.33
2 + 1 R	1.47	16.9	-	9.7×10^{-3}	-	17.2	0.24	0.67	1.68	0.42
3 + 1 R	1.38	17.9	-	7.4×10^{-3}	-	18.6	0.22	0.58	1.42	0.37
4 + 1 R	1.32	19.0	-	5.8×10^{-3}	-	19.5	0.21	0.52	1.28	0.33
2 + 1 TP	1.40	22.7	-	6.0×10^{-3}	2.93	18.8	0.30	0.66	1.14	0.40
3 + 1 TP	1.30	48.2	-	6.0×10^{-3}	7.36	34.7	0.26	0.61	1.07	0.38
4 + 1 TP	1.37	46.4	-	6.0×10^{-3}	8.78	35.5	0.24	0.58	1.01	0.37
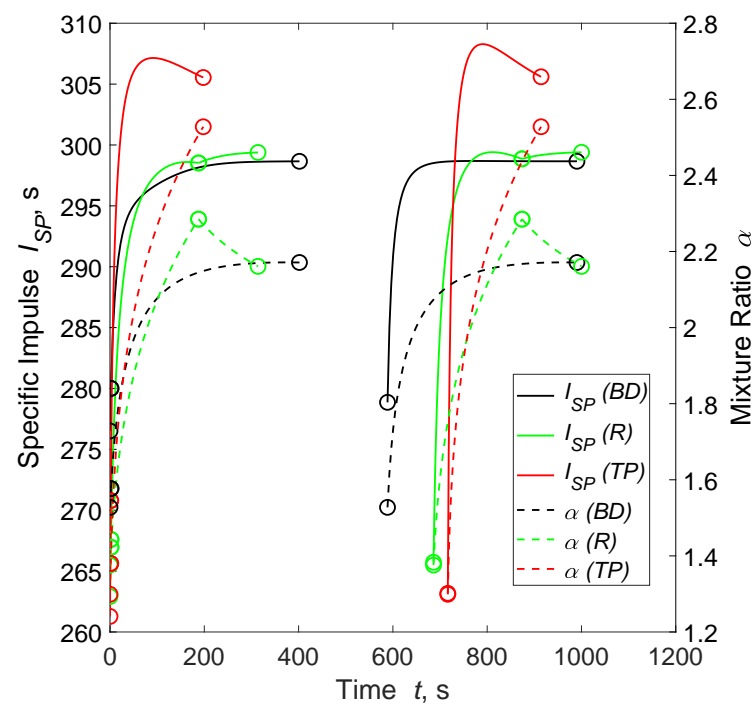
Figure 2. Specific impulse I_{SP} and mixture ratio α histories for the best solution of each feed system. The BD solution was obtained with $N_1 = 2$ and R and TP solutions with $N_1 = 3$.
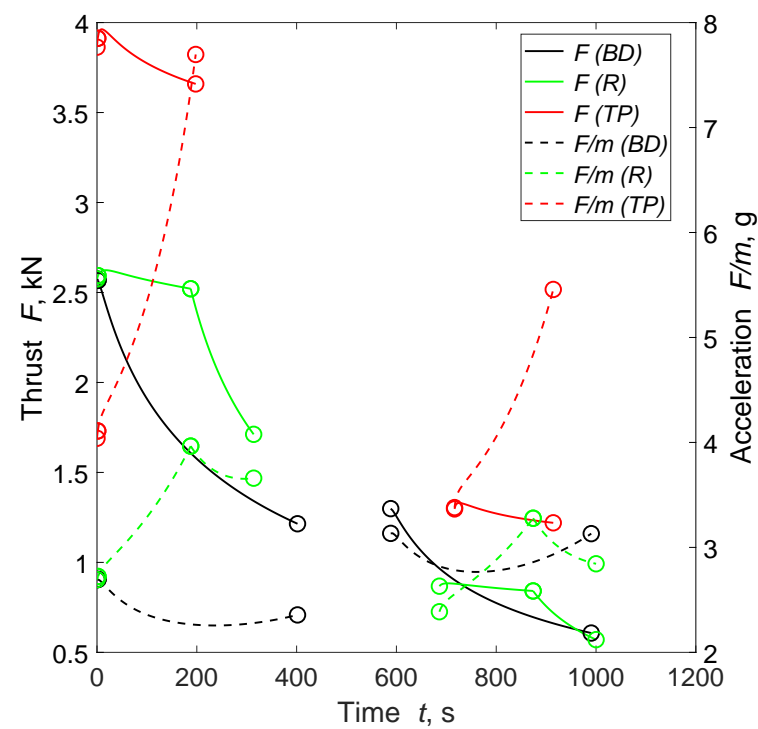
Figure 3. Thrust F and longitudinal acceleration F/m histories for the best solution of each feed system. The BD solution was obtained with $N_1 = 2$ and R and TP solutions with $N_1 = 3$.
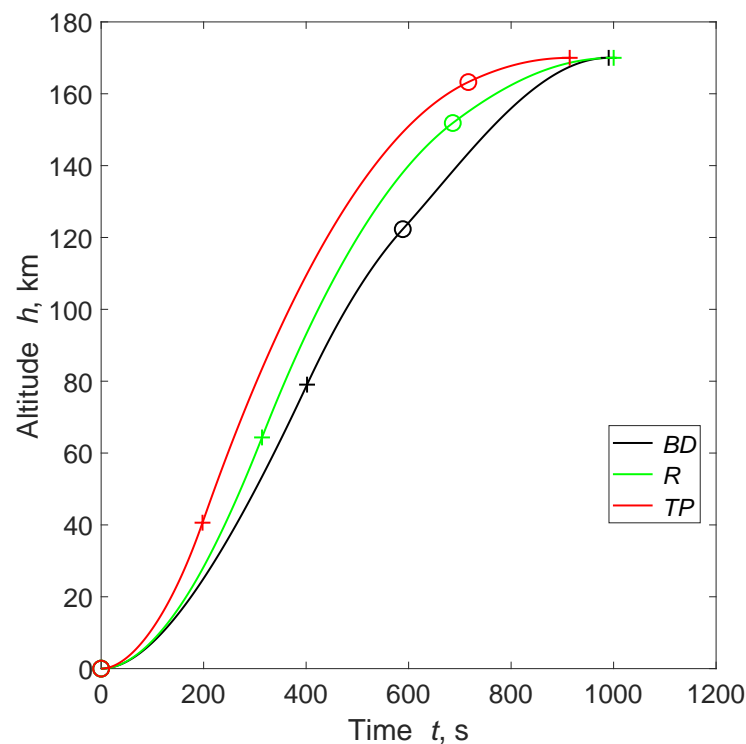
Figure 4. Trajectory for the best solution of each feed system. The BD solution was been obtained with $N_1 = 2$ and R and TP solutions with $N_1 = 3$. The dots and crosses represent the stages ignition and burnout, respectively.

5. Conclusions

In this work, the design and optimization of a HRE suitable for a MAV have been analyzed in the context of a sample return mission. A multi-disciplinary approach has been employed: an indirect method optimizes the ascent trajectory given the engine design, which is in turn optimized by a direct optimization method. Several feed system options and first-stage configurations have been taken into account and the resulting performance compared. The results demonstrated the feasibility of a hybrid MAV concept, being the payload masses comparable to those provided by heritage LREs envisaged for such mission. Hence, hybrids are an option worth considering, also taking into account their intrinsic simplicity and low cost. The results also show that the use of an electric turbo-pump feed system is able to grant a remarkable increase in payload, although issues related to the lower technological readiness level, with respect to more consolidated feed systems, should be considered. The proposed procedure represents a powerful and efficient means for a preliminary but accurate design and estimation of performance of the hybrid propulsion system. The time required by the whole computation is relatively short even on an everyday personal computer, making the procedure suitable for fast evaluation of trade-offs. In order to increase the accuracy of this approach, future developments will include more precise aerodynamic modeling of the subrockets and structural weights estimation alongside a throat erosion model.

Author Contributions: Conceptualization, L.C., F.M. and D.P.; Formal analysis, L.C., F.M. and D.P.; Methodology, L.C., F.M. and D.P.; Supervision, L.C. and D.P.; Writing—original draft, F.M.; Writing—review and editing, L.C., F.M. and D.P. All authors have read and agreed to the published version of the manuscript.

Abbreviations

The following abbreviations are used in this manuscript:

BD   Blow Down
LRE(s)   Liquid Rocket Engine(s)
LOX   Liquid OXygen
MAV   Mars Ascent Vehicle
R   Regulated
RHS   Right-Hand Side
SRM(s)   Solid Rocket Motor(s)
TP   Turbo Pump

Nomenclature

A_b burning surface area, m^2
A_p port area, m^2
A_{th} nozzle throat area, m^2
a regression constant, m^{1+2n} kg^{-n} s^{n-1}
C_F thrust coefficient
c^* characteristic velocity, m/s
$\boldsymbol{D}$ drag vector, N
d rocket outer diameter, m
$\boldsymbol{F}$ thrust vector, N
F thrust, N
G gravitational constant, Nm^2/kg^2
$\boldsymbol{g}$ gravity acceleration, m/s^2
H Hamiltonian
h altitude, km
I_{SP} mean specific impulse, s
J throat area to initial port area ratio
L overall engine length, m
L_b fuel grain length, m
M rocket mass, kg
m mass, kg
N_1 engines number in the first stage
n mass-flux exponent
P_e electric power, kW
p pressure, bar
$\boldsymbol{r}$ position vector, m
t time, s
T temperature, K
V volume, m^3
$\boldsymbol{v}$ velocity vector, m/s
w web thickness, m
y burning distance, m
Z hydraulic resistance, 1/(kg m)
α mixture ratio
γ specific heat ratio
δ_{ep} electric motor and pump power density, kW/kg
δ_{be} batteries energy density, Wh/kg
δ_{bp} batteries power density, kW/kg
ϵ nozzle area ratio
η_{ep} electric motor and pump efficiency
λ adjoint variable
μ payload, kg
ρ density, kg/m^3

Superscripts

$\cdot$	time derivative
$*$	characteristic

Subscripts

1	combustion chamber at head-end
atm	atmospheric
avg	average
cc	combustion chamber
d	discharge
dry	dry
e	nozzle exit
ep	electric motor and pump
F	fuel
f	final
fs	feed system
i	initial value
max	maximum
min	minimum
n	nozzle
O	oxidizer
p	overall propellant (oxidizer + fuel)
rel	relative
res	residual
t	oxidizer propellant tank
th	throat
tot	total

References

1. Casalino, L.; Pastrone, D. Optimal Design of Hybrid Rocket Motors for Microgravity Platform. *J. Propuls. Power* **2008**, *24*, 491–498. [CrossRef]
2. Casalino, L.; Pastrone, D. Optimal Design of Hybrid Rocket Motors for Launchers Upper Stages. *J. Propuls. Power* **2010**, *26*, 421–427. [CrossRef]
3. Casalino, L.; Pastrone, D. Optimization of Hybrid Sounding Rockets for Hypersonic Testing. *J. Propuls. Power* **2012**, *28*, 405–411. [CrossRef]
4. Chandler, A.; Cantwell, B.; Hubbard, G.S.; Karabeyoglu, A. A Two-Stage, Single Port Hybrid Propulsion System for a Mars Ascent Vehicle. In Proceedings of the 46th AIAA/ASME/SAE/ASEE Joint Propulsion Conference & Exhibit, Nashville, TN, USA, 25–28 July 2010. [CrossRef]
5. Chandler, A.A.; Cantwell, B.J.; Hubbard, G.S.; Karabeyoglu, A. Feasibility of a Single Port Hybrid Propulsion System for a Mars Ascent Vehicle. *Acta Astronaut.* **2011**, *69*, 1066–1072. [CrossRef]
6. Sopegno, L.; Valavanis, K.P.; Rutherford, M.J.; Casalino, L. Mars Sample Return Mission: Mars Ascent Vehicle Propulsion Design. In Proceedings of the 2020 IEEE Aerospace Conference, Big Sky, MT, USA, 7–14 March 2020; IEEE: Piscataway, NJ, USA, 2020; pp. 1–9. [CrossRef]
7. McCollum, L.T.; Schnell, A.; Yaghoubi, D.; Bean, Q.; McCauley, R.; Prince, A. Development Concepts for Mars Ascent Vehicle (MAV) Solid and Hybrid Vehicle Systems. In Proceedings of the 2019 IEEE Aerospace Conference, Big Sky, MT, USA, 2–9 March 2019; IEEE: Piscataway, NJ, USA, 2019; pp. 1–10. [CrossRef]
8. Karp, A. Hybrid Rocket Propulsion for a Low Temperature Mars Ascent Vehicle. In Proceedings of the Lecture Held at Jet Propulsion Laboratory, National Aeronautics and Space, Pasadena, CA, USA, 13 March 2017.
9. Oglesby, B.; Prince, A.; Story, G.; Kam, A. Qualification of a Hybrid Propulsion System for a Mars Ascent Vehicle. In Proceedings of the 2019 IEEE Aerospace Conference, Big Sky, MT, USA, 2–9 March 2019; IEEE: Piscataway, NJ, USA, 2019; pp. 1–7.
10. Evans, B.; Cantwell, B. Development and testing of SP7 fuel for mars ascent vehicle application. In Proceedings of the 2019 IEEE Aerospace Conference, Big Sky, MT, USA, 2–9 March 2019; IEEE: Piscataway, NJ, USA, 2019; pp. 1–11.
11. Muirhead, B.K.; Karp, A. Mars Sample Return Lander Mission Concepts. In Proceedings of the 2019 IEEE Aerospace Conference, Big Sky, MT, USA, 2–9 March 2019; IEEE: Piscataway, NJ, USA, 2019; pp. 1–9.
12. Drake, B.G. (Ed.) *Human Exploration of Mars Design Reference Architecture 5.0*; NASA-SP-2009-566; NASA: Washington, DC, USA, 2009.
13. Boiron, A.J.; Cantwell, B. Hybrid Rocket Propulsion and in situ Propellant Production for Future Mars Missions. In Proceedings of the 49th AIAA/ASME/SAE/ASEE Joint Propulsion Conference, San Jose, CA, USA, 14–17 July 2013; p. 3899. [CrossRef]

14. Shotwell, R.; Benito, J.; Karp, A.; Dankanich, J. Drivers, developments and options under consideration for a Mars ascent vehicle. In Proceedings of the 2016 IEEE Aerospace Conference, Big Sky, MT, USA, 5–12 March 2016; IEEE: Piscataway, NJ, USA, 2016; pp. 1–14.

15. Casalino, L.; Pastrone, D. Optimal Design and Control of Hybrid Rockets for Access to Space. In Proceedings of the 41st AIAA/ASME/SAE/ASEE Joint Propulsion Conference and Exhibit, Tucson, AZ, USA, 10–13 July 2005. [CrossRef]

16. Pastrone, D.; Casalino, L. Optimal Robust Design of Hybrid Rocket Engines. In *Space Engineering*; Springer: Berlin/Heidelberg, Germany, 2016; Volume 114, pp. 269–285. [CrossRef]

17. Casalino, L.; Masseni, F.; Pastrone, D. Robust Design Approaches for Hybrid Rocket Upper Stage. *J. Aerosp. Eng.* **2019**, *32*. [CrossRef]

18. Casalino, L.; Masseni, F.; Pastrone, D. Uncertainty Analysis and Robust Design for a Hybrid Rocket Upper Stage. *J. Spacecr. Rockets* **2019**, *56*, 1424–1431. [CrossRef]

19. Casalino, L.; Pastrone, D. Optimization of Hybrid Propellant Mars Ascent Vehicle. In Proceedings of the 50th AIAA/ASME/SAE/ASEE Joint Propulsion Conference, Cleveland, OH, USA, 28–30 July 2014. [CrossRef]

20. Casalino, L.; Pastrone, D. Optimization of a Hybrid Rocket Upper Stage with Electric Pump Feed System. In Proceedings of the 46th AIAA/ASME/SAE/ASEE Joint Propulsion Conference & Exhibit, Nashville, TN, USA, 25–28 July 2010. [CrossRef]

21. Casalino, L.; Masseni, F.; Pastrone, D. Viability of an Electrically Driven Pump-fed Hybrid Rocket for Small Launcher Upper Stages. *Aerospace* **2019**, *6*, 36. [CrossRef]

22. Morring, F.J.; Norris, G. Rocket Lab Unveils Battery-Powered Turbomachinery. Available online: http://aviationweek.com/space/rocket-lab-unveils-battery-powered-turbomachinery (accessed on 21 June 2021).

23. Bailey, M. Frequent and Reliable Launch for Small Satellites: Rocket Lab's Electron Launch Vehicle and Photon Spacecraft. In *Handbook of Small Satellites: Technology, Design, Manufacture, Applications, Economics and Regulation*; Springer: Berlin/Heidelberg, Germany, 2020; pp. 1–17.

24. Gegeoglu, K.; Kahraman, M.; Ucler, C.; Karabeyoglu, A. Assessment of using electric pumps on hybrid rockets. In Proceedings of the AIAA Propulsion and Energy 2019 Forum, Indianapolis, IN, USA, 19–22 August 2019. [CrossRef]

25. Casalino, L.; Letizia, F.; Pastrone, D. Design Trade-offs for Hybrid Rocket Motors. In Proceedings of the 48th AIAA/ASME/SAE/ASEE Joint Propulsion Conference and Exhibit, Atlanta, GA, USA, 30 July–1 August 2012. [CrossRef]

26. Casalino, L.; Letizia, F.; Pastrone, D. Optimization of Hybrid Upper-Stage Motor with Coupled Evolutionary/Indirect Procedure. *J. Propuls. Power* **2014**, *30*. [CrossRef]

27. McBride, B.J.; Reno, M.A.; Gordon, S. *CET93 and CETPC: An Interim Updated Version of the NASA Lewis Computer Program for Calculating Complex Chemical Equilibria with Applications*; NASA TM-4557; NASA: Washington, DC, USA, 1994.

28. Sutton, G.P.; Biblarz, O. *Rocket Propulsion Elements*; John Wiley & Sons: Hoboken, NJ, USA, 2001.

29. Maisonneuve, V.; Godon, J.; Lecourt, R.; Lengelle, G.; Pillet, N. Hybrid Propulsion for Small Satellites Design Logic and Tests. *Int. J. Energ. Mater. Chem. Propuls.* **2002**, *5*. [CrossRef]

30. Schoonover, P.; Crossley, W.A.; Heister, S. Application of a Genetic Algorithm to the Optimization of Hybrid Rockets. *J. Spacecr. Rockets* **2000**, *37*, 622–629. [CrossRef]

31. Barrere, M.; Jaumotte, A.; Fraeijs de Veubeke, B.; Vandenkerckhove, J. *Rocket Propulsion*; Elsevier: Amsterdam, The Netherlands, 1960.

32. Kwak, H.D.; Kwon, S.; Choi, C.H. Performance Assessment of Electrically Driven Pump-fed LOX/Kerosene Cycle Rocket Engine: Comparison with Gas Generator Cycle. *Aerosp. Sci. Technol.* **2018**, *77*, 67–82. [CrossRef]

33. Barker, D.; Belnap, R.; Hall, A.; Kordig, J. A Simplified Method of Predicting Char Formation in Ablating Rocket Exit Cones. In *Chemical Engineering Progress, Symposium Series*; American Institute of Chemical Engineers: New York, NY, USA, 1965; Volume 61, pp. 108–114.

34. Casalino, L.; Pastrone, D. Oxidizer Control and Optimal Design of Hybrid Rockets for Small Satellites. *J. Propuls. Power* **2005**, *21*, 230–238. [CrossRef]

35. Casalino, L.; Colasurdo, G.; Pastrone, D. Optimal Low-Thrust Escape Trajectories Using Gravity Assist. *J. Guid. Control Dyn.* **1999**, *22*, 637–642. [CrossRef]

36. Colasurdo, G.; Pastrone, D. Indirect Optimization Method for Impulsive Transfers. In Proceedings of the Astrodynamics Conference, Scottsdale, AZ, USA, 1–3 August 1994; pp. 441–448. [CrossRef]